Morphology and Structure of CuO_x/CeO_2 Nanocomposite Catalysts Produced by Inert Gas Condensation: An HREM, EFTEM, XPS, and High-Energy Diffraction Study

B. Skårman,*,† T. Nakayama,‡ D. Grandjean,§ R. E. Benfield,§ E. Olsson,|| K. Niihara,‡ and L. R. Wallenberg†

Department of Materials Chemistry, National Center for HREM, Lund University, P.O. Box 124, S-22100 Lund, Sweden, Institute of Scientific and Industrial Research (ISIR), Osaka University, Osaka, Japan, Centre for Materials Research, School of Physical Sciences, University of Kent, Canterbury CT2 7NR, United Kingdom, and Department of Materials Science, The Ångström Laboratory, Uppsala University, Uppsala, Sweden

Received January 11, 2002. Revised Manuscript Received June 11, 2002

Inert gas condensation (IGC) has been employed to produce nanoparticles of the low-temperature combustion catalyst CuO_x/CeO_2. For the first time we have used a multiple heating crucible setup to tailor various morphologies over the whole compositional range (2−98% Cu). The factors that control the growth, structure, and morphology of the nanocomposite have been studied. A powerful combination of complementary characterization methods has been used to elucidate the catalytic synergistics of this material. Investigations by high-resolution transmission electron microscopy (HRTEM) and energy-filtered TEM (EFTEM) are supported by X-ray photoelectron spectroscopy (XPS) and high-energy diffraction (HED) measurements. The nonstoichiometric CuO_x/CeO_2 composite displays an amorphous character consisting of aggregated CeO_2 (ceria) nanocrystallites over which amorphous copper clusters (or a thin film of a solid solution) are finely dispersed. In the range 6∼20% Cu, copper is predominantly located at the surface, which can give the material optimum catalytic properties. Development of crust structures, for example, core−shells, are formed in the 30∼70% Cu concentration range and is attributable to a sequential oxidation of Ce followed by Cu and an ideal proportion of lattice expansion for the oxides. We suggest a model that illustrates the formation of the crust structure and may explain the observed extreme dispersion of copper on ceria. The helium gas pressure during the thermalization controls the crystal size and the degree of crystallite aggregation. Rounded particle shapes consisting of epitaxially interfaced nanocrystallites exhibit an X-ray amorphous character, while block-shaped crystals displaying sharp edges and distinct flat surfaces give rise to a higher X-ray crystallinity. Bulk CuO crystals were detected by high-energy diffraction above a 30% Cu content. However, the extreme copper dispersion is preserved even for higher copper contents, showing no limit of surface saturation.

1. Introduction

Ceria has been widely used as an additive in heterogeneous industrial catalysts[1] and in the automotive three-way catalytic (TWC) converter as an oxygen storage medium and thermal stabilizer.[2,3] It is clear that the presence of mixed valence states (3+/4+) in ceria is important for its high catalytic activity because it permits the reversible addition and removal of oxygen from its fluorite structure.[4−6] It is well-known that ceria is not just an inert carrier for supported species but also a modifier affecting the degree of dispersion as well as the physiochemical properties (e.g., adsorption, catalytic activity, redox behavior, and magnetic behavior) of the supported species.

We have today the technology to grow and control structures on the nanometer scale, which has opened the possibility to fabricate novel materials with unique physical and chemical properties.[7,8] For example, inert gas condensation (IGC) has previously been utilized to produce stable nonstoichiometric cerium oxides by first synthesizing metallic nanometer-sized clusters followed by controlled oxidation.[9−11] It has been shown that this

* To whom correspondence should be addressed. E-mail: bjorn.skarman@materialkemi.lth.se. Fax: (46) 46 222 4012.
† Lund University.
‡ Osaka University.
§ University of Kent.
|| Uppsala University.

(1) Trovarelli, A.; de Leitenburg, C.; Boaro, M.; Dolcetti, G. *Catal. Today* **1999**, *50*, 353.
(2) Bunluesin, T.; Gorte R. J.; Graham, G. W. *Appl. Catal. B* **1997**, *14*, 105.
(3) Holmgren, A. Ph.D. Thesis, Chalmers University of Technology, Gothenburg, Sweden, 1998.
(4) Lamonier, C.; Wrobel, G.; Bonnelle, J. P. *J. Mater. Chem.* **1994**, *4*, 1927.
(5) Conesa, J. C. *Surf. Sci.* **1995**, *339*, 337.
(6) Trovarelli, A. *Catal. Rev.* **1996**, *38*, 439.
(7) Wolde, A. T. *Nanotechnology−towards a molecular construction kit*; STT: The Hague, The Netherlands, 1998.
(8) Moser, W. R. *Advanced catalysts and nanostructured materials*; Academic Press: San Diego, CA, 1996.
(9) Ying, J. Y.; Tschöpe, A.; Levin, D. *Nanostruct. Mater.* **1995**, *6*, 237.

10.1021/cm021101u CCC: $22.00
Published on Web 08/22/2002

nanocrystalline material exhibits significantly improved catalytic properties compared to its coarse-grained counterpart.[12,13] The larger portion of surface atoms in these exceptionally small crystallites can explain, because of a surface energy relaxation process, the preserved reduced state.[5,14−16]

Copper, or copper oxide, on ceria is known for its high catalytic activity in CO oxidation and CH_4 hydrogenolysis,[17] SO_2 reduction by CO,[18] NO reduction,[19,20] methanol synthesis,[21] and catalytic wet oxidation (CWO) of phenol.[22,23] This type of composite catalyst also shows excellent resistance to carbon dioxide, water poisoning, and sulfur compounds.[24] It is not entirely clear how the supported copper species enhance the catalytic performance, although the ease with which oxygen vacancies are created in the support material (enthalpy of vacancy formation) appears to be strongly influenced by the copper presence through a synergistic mechanism. We have previously shown[25] that copper oxide exhibits a dramatically improved activity for the oxidation of carbon monoxide on CeO_2{001} surfaces, compared to the dominating low-energy CeO_2{111}, because of its ability to assist the copper oxide in changing valence and supplying oxygen. Hence, if the properties of the active oxygen species can be controlled, it would be possible to design the oxidative properties of the catalyst.[26] The choice of preparation method appears to greatly control the predominant form and distribution of the copper species on ceria. Gas-phase-produced Cu/Ce metal clusters upon oxidation, however, have only been observed,[9,10,27,28] to be transferred into, what could be called, a disordered solid oxide matrix, with the absence of intermetallic phases or bulk solid solutions. Bulk CuO was shown to be formed only upon annealing at elevated temperatures.

By employing the inert gas condensation (IGC) technique, almost any metal can be used to produce composites with a wide range of different compositions.[29] It also provides the possibility to alter the nanosized morphology, the crystallinity, and particle size.[11,30] Yet another advantage of the IGC method is that, because of the nature of the vapor condensation growth process, a larger portion of internal interfaces and grain boundaries with a high degree of cleanliness between the metals can be obtained,[31] which is known to be a prerequisite for obtaining highly active catalysts.

The aim of this study was to obtain a better understanding of which factors control the growth and morphology of the CuO_x/CeO_2 composite, for the first time studied over the whole compositional range (2−98%), and to seek the most favorable nanosized morphology from a catalytic point of view. In this first descriptive paper we focus on growth and characterization of this composite catalyst. In a following paper the catalytic results will be evaluated and discussed in combination with additional XAS measurements.[32] The characterization is primarily based on high-resolution transmission electron microscopy (HRTEM) and energy-filtered TEM (GIF). The results of X-ray photoelectron spectroscopy (XPS) and high-energy diffraction (HED) using synchrotron radiation will be discussed in comparison to the TEM evaluation.

2. Experimental Section

2.1. Catalyst Synthesis. The catalyst powders of CuO_x/CeO_2 were synthesized by inert gas condensation (IGC) utilizing resistive heating evaporation. Pure metallic cerium and copper granules (Kojundo Chemical Lab. Co. Ltd.) were used as source materials and evaporated simultaneously in two or three resistively heated tungsten crucibles. After pumping down to UHV conditions ($<10^{-9}$ Torr), the chamber is filled with a low pressure of inert helium gas. The evaporated metallic monomers are cooled by collisions with the "cold" inert helium gas atoms and aggregate into clusters from collisions between monomers. The produced particle size can be manipulated by the gas pressure or by the evaporation rate. Helium pressures of 0.5, 1.0, 5.0, and 10.0 Torr were tested. The aerosol of particles is transported via self-induced thermal convective flux to a cylindrical liquid N_2-cooled rotating coldfinger, where it is continuously collected.[33] After the evaporation the UHV was restored and then slowly back-filled with oxygen to a final pressure of 1.0 Torr. The oxidized material was scraped off from the coldfinger and was characterized in this as-prepared powder form. The treatment and storage in gastight glass cylinders have been identical for all samples. More information about the advantages and limitations of the IGC method can be obtained elsewhere.[8,11,34,35]

2.2. Characterization. *2.2.1. High-Resolution Electron Microscopy (HREM).* The majority of the samples were characterized in a JEM 4000EX high-resolution transmission electron microscope (HRTEM). The microscope has a structural resolving power of 1.6 Å at an accelerating voltage of 400 kV. A JEM 3000F high-resolution field-emission transmission electron microscope (located at ISIR, Osaka University, Japan) was used to examine some of the samples immediately after the synthesis.

(10) Ying, J. Y.; Tschöpe, A. *Chem. Eng. J.* **1996**, *64*, 225.
(11) Guillou, N.; Nistor L. C.; Fuess, H.; Hahn, H. *Nanostruct. Mater.* **1997**, *8*, 545.
(12) Lavik, E. B.; Chiang, Y.-M. *Mater. Res. Soc. Symp. Proc.* **1997**, *457*, 63.
(13) Tschöpe, A.; Liu, W.; Flytzani-Stephanopoulos, M.; Ying, J. Y. *J. Catal.* **1995**, *157*, 42.
(14) Baudin, M. Ph.D. Thesis, Uppsala University, Uppsala, Sweden, 2000.
(15) Sayle, T. X. T.; Parker, S. C.; Catlow R. A. *Surf. Sci.* **1994**, *316*, 329.
(16) Cordatos, H.; Ford, D.; Gorte, R. J. *J. Phys. Chem.* **1996**, *100*, 18128.
(17) Liu, W.; Flytzani-Stephanopoulos, M. *J. Catal.* **1995**, *153*, 304−332 (Parts I and II).
(18) Zhu, T.; Kundakovic, L.; Dreher, A.; Flytzani-Stephanopoulos, M. *Catal. Today* **1999**, *50*, 381.
(19) Bera, P.; Mitra, S.; Sampath, S.; Hegde, M. S. *Chem. Commun.* **2001**, 927.
(20) Fernández-García, M.; Rebollo, G. E.; Ruiz, A. G.; Conesa, J. C.; Soria, J. *J. Catal.* **1997**, *172*, 146.
(21) Shaw, E. A.; Rayment, T.; Walker, A. P.; Lambert, R. M.; Gauntlett, T.; Oldman, R. J.; Dent, A. *Catal. Today* **1991**, *9*, 197.
(22) Hocevar, S.; Batista, J.; Levec, J. *J. Catal.* **1999**, *184*, 39.
(23) Hocevar, S.; Krasovec, U. O.; Orel, B.; Arico, A. S.; Kim, H. *Appl. Catal. B* **2000**, *28*, 113.
(24) Liu, W.; Sarofim, A. F.; Flytzani-Stephanopoulos, M. *Appl. Catal. B* **1994**, *4*, 167.
(25) Skårman, B.; Wallenberg, L. R.; Larsson, P.-O.; Andersson, A.; Bovin, J.-O.; Jacobsen, S. N.; Helmersson, U. *J. Catal.* **1999**, *181*, 6.
(26) Satterfield, C. N. *Heterogeneous catalysis in industrial practice*, 2nd ed.; Krieger Publishing Co.: Malabar, FL, 1996.
(27) Skårman, B.; Nakayama, T.; Niihara, K.; Wallenberg, L. R. *Microsc. Microanal. Proc.* **2001**, *7*, 1074.
(28) Nakayama, T.; Skårman, B.; Wallenberg, L. R.; Sekino, T.; Choa, Y.-H.; Yamamoto, T. A.; Niihara, K. *Scr. Mater.* **2001**, *44*, 1929.
(29) Granqvist, C. G.; Buhrman, R. A. *J. Appl. Phys.* **1976**, *47*, 2200.
(30) Nakayama, T.; Yamamoto, T. A.; Choa, Y.-H.; Niihara, K. *J. Mater. Sci.* **2000**, *35*, 3857.
(31) Birringer, R.; Gleiter, H.; Klein, H. P.; Marquardt, P. *Phys. Lett. A* **1984**, *102*, 365.
(32) Skårman, B.; Hinz, A.; Grandjean, D.; Benfield, R. E.; Wallenberg, L. R. *J. Catal.*, in press (DOI: 10.1006/jcat.2002.3735).
(33) Siegel, R. W. *Annu. Rev. Mater. Sci.* **1991**, *21*, 559.
(34) Gleiter, H. *Prog. Mater. Sci.* **1989**, *33*, 223.
(35) Averback, R. S.; Hahn, H.; Höfler, H. J.; Logas, J. L.; Shen, T. C. *Mater. Res. Soc. Symp. Proc.* **1989**, *153*, 3.

Table 1. Influence of Helium Pressure during IGC Synthesis on Crystal Size and Particle Size (Std. Dev. in Parentheses)

He pressure (Torr)	D_β (nm)	D_{TEM} (nm)	S_{BET}[a] (m^2/g)
0.5; 1.0	8(2)	9(2)	69
5.0	12(2)	18(4)	31
10.0	12(4)	45(9)	28

[a] The BET-area values are from the three specific samples displayed in Figure 3.

2.2.2. Energy-Filtered Transmission Electron Microscopy (EFTEM). A FEI Technai 300-kV field-emission TEM (located at the Ångström Laboratory, Uppsala University, Sweden) equipped with a Gatan image filter (GIF) was used for the high-resolution elemental mapping. The microscope has a structural resolving power of 1.9 Å and chemical information can be obtained with a resolution of less than 1 nm. For lower magnifications a Philips CM120 BioTWIN Cryo operated at 120 kV, also equipped with a GIF, was used for chemical mapping of the catalyst powders. This microscope has a point-to-point resolution of 3.4 Å.

2.2.3. X-ray Energy-Dispersive Spectrometry (XEDS). A JSM-840A scanning electron microscope, interfaced with a Link AN10000 X-ray energy-dispersive microanalysis system, was used to determine the bulk composition. The copper content for the powder samples will be defined as % Cu throughout the paper, calculated according to $n_{Cu}/(n_{Cu} + n_{Ce}) \times 100\%$. A peak-to-background calculation software (PB-Quant) was used to quantify the composition over the rough powder surfaces.

2.2.4. Specific Surface Area. The specific surface areas (S_{BET}) were obtained from multipoint Brunauer−Emmet−Teller (BET) analysis of nitrogen adsorption (Micrometrics ASAP 2400). All samples were degassed at 373 K for 24 h before analysis. The particle size (D_{BET}) was calculated from the BET measurements assuming a spherical shape using the following expression,[36]

$$D_{BET} = \frac{6 \times 10^4}{(\rho \times S_{BET})}$$

where ρ is the theoretical density of CeO_2 (7.21 g/cm^3) and S_{BET} is expressed in m^2/g.

2.2.5. X-ray Photoelectron Spectroscopy (XPS). X-ray photoelectron spectroscopy analyses were performed on a Kratos XSAM 800 spectrometer using Al Kα radiation (1486.6 eV). Charging effects were corrected by adjusting the C 1s peak to a position of 285.0 eV. Because of the photoreduction of the dispersed copper oxide[17,37,38] or noncrystalline cerium oxide[39] in the spectrometer, the analysis of each sample was initiated with single-scan analysis of the Cu 2p, Ce 3d, C 1s, and O 1s regions, in that order (total 13 min), followed by wide-scan analysis (5 min) between 0- and 1100-eV binding energy. The pass energy was set to 40 eV for the region scans and 80 eV for the wide scan analysis.

2.2.6. High-Energy Diffraction (HED). The high-energy diffraction measurements were carried out on beamline ID15B at the European Synchrotron Radiation Facility (ESRF), Grenoble, France, operating under beam conditions of 6 GeV, 80 mA, and 2/3 filling mode using an X-ray energy of 89 keV corresponding to a wavelength of 0.1387 Å. The beam size was 100×100 μm at the sample and the flux from the Bragg-type monochromator about 10^{12} photons/s. Further details about the beamline can be found elsewhere.[40] The powder samples were contained in ultrapure amorphous silicon capillary tubes (Ø 3 mm), mounted horizontally perpendicular to the X-ray beam. The high-quality diffraction profiles were collected on a two-dimensional (2D) image plate detector using data collection times of 20 min for the IGC-powder samples and 5 min for the reference samples. The 2D-diffraction patterns were radially integrated using the FIT2D software package[41] to display the intensity profile as a function of the 2θ scattering angle.

The mean crystallite sizes of the CeO_2 grains were determined from line-broadening measurements on the ⟨111⟩, ⟨220⟩, and ⟨311⟩ peaks of CeO_2, using the Scherrer equation,[42]

$$D_\beta = \frac{K\lambda}{\beta \cos \theta}$$

where λ is the synchrotron wavelength, K is the particle shape factor, taken as 1.025 for spherical particles,[43] and β is the full-width at half-maximum (fwhm) in radians. The β-values were carefully determined by a least-squares fit of a Gaussian function. Deconvolution of the instrumental line broadening, as determined from a microcrystalline copper metal reference sample, yielded a physical peak width.

By converting the diffraction angle 2θ into reciprocal space variable $s = 2 \sin \theta/\lambda$, one can show[43] that the peak broadening $(\delta s)_{size}$ due to size effects is independent of s, while the strain broadening $(\delta s)_{strain}$ is proportional to s. Thus, the dependence of the measured peak width $(\delta s)_0$, determined after instrumental broadening corrections, on s enables the broadening contributions of size and strain effects to be distinguished. Using a Cauchy/Gaussian convolution, one finds according to the Stokes−Wilson equations,[43−45] that the relationship between the volume-averaged crystal size D_s and the root-mean-square strain $\langle e^2 \rangle^{1/2}$ is

$$\frac{1}{(\delta s)_0} \approx D_s - 6.25\langle e^2 \rangle D_S \left[\frac{s}{(\delta s)_0}\right]^2$$

By plotting $1/(\delta s)_0$ against $[s/(\delta s)_0]^2$ for six diffraction peaks, we were able to determine D_s and rms $\langle e^2 \rangle^{1/2}$. The D_s crystal size is in accordance with the Scherrer mean crystal size (D_β), but inherits a larger statistical error.

3. Results and Discussion

A total number of 50 samples have been synthesized and examined, but we have in this paper chosen to select only a few samples for presentation that suitably represent all the observed morphologies.[46] In Tables 1 and 2 are data gathered of some of the selected samples that are described in the text. We have focused our investigation from the following viewpoints that might influence the catalytic activity:

(i) The parameters of inert gas-phase synthesis affecting the nanosized morphology, for example, the helium pressure and the crucible setup (IGC, HREM).

(ii) The composition and its dependency on the composite morphology (HREM, XEDS).

(iii) The crystallite size, crystallinity, and particle morphology (HREM, HED).

(iv) Copper dispersion phenomena and interfacial solid solutions (HREM, XPS, HED).

(36) Audebrand, N.; Auffredic, J.-P.; Louër, D. *Chem. Mater.* **2000**, *12*, 1791.
(37) Larsson, P.-O.; Andersson, A.; Wallenberg, L. R.; Svensson, B. *J. Catal.* **1996**, *163*, 279.
(38) Harrison, P. G.; Ball, I. K.; Azalee, W.; Daniell, W.; Goldfarb, D. *Chem Mater.* **2000**, *12* (12), 3715.
(39) Park, P. W.; Ledford, J. S. *Langmuir* **1996**, *12*, 1794.
(40) http://www.esrf.fr/exp_facilities/ID15B/home/id15home.html, accessed Jan 2001.
(41) Hammersley, A. *FIT2D software*; ESRF: Grenoble, 1995.
(42) Scherrer, P. *Göttlische Nachrichten* **1918**, *2*, 98.
(43) Klug, H. P.; Alexander, L. E. *X-ray diffraction procedures for polycrystalline and amorphous materials*, 2nd ed.; John Wiley & Sons Inc.: New York, 1974.
(44) Stokes, A. R.; Wilson A. J. C. *Proc. Phys. Soc. (London)* **1944**, *56*, 174.
(45) Eckert, J.; Holzer, J. C.; Krill, C. E.; Johnson, W. L. *J. Mater. Res.* **1992**, *7*, 1751.
(46) Skårman, B. Ph.D. Thesis, Lund University, Lund, Sweden, 2002.

Table 2. BET, HED, and TEM Data for a Selection of the Examined IGC-Produced CuO_x/CeO_2 Samples

	He pressure (Torr)	Cu content[a] (%)	S_{BET} (m^2/g^1)	D_β (nm)	D_{TEM} particle size (nm)	D_{BET}[b] (nm)	$\langle D_{BET}/D_\beta \rangle^3$ c	cryst. factor I_P/I_B	unit cell parameter (nm)
				Low Cu Contents					
CeO_2-ref.		0	3.7	45.4	92(10)	223	119	(0.954)	0.54145
A1	5.0	2.8	30.7	13.1	25(4)	27.2	27	0.187	0.54175
A2	1.0	3.2	41.2	9.7	18(3)	20.3	20	0.259	0.54167
A3	0.5	4.5	42.2	11.4	18(3)	19.8	13	0.290	0.54196
A4	5.0	4.9	36.6	11.3	23(5)	22.8	15	0.051	0.54222
				Medium Cu Contents					
B1	1.0	6.1	36.0	12.4	13(2)	23.3	23	0.388	0.54201
B2	1.0	11.5	52.7	7.7	14(2)	16.0	15	0.170	0.54158
B3	0.5	13.0	39.5	9.2	11(2)	21.3	27	0.395	0.54244
B4	1.0	13.1	58.6	8.1	15(2)	14.4	10	0.209	0.54189
				High Cu Contents					
C1	1.0	29.4	59.4	5.3	10(2)	14.4	24	0.172	0.54206
C2	1.0	54.0	55.3	6.5	13(2)	15.9	21	0.168	0.54104
C3	1.0	68.0	111.1	6.8	8(2)	8.0	3	0.140	0.54187

[a] Atomic percentage of Cu related to Ce. [b] $D_{BET} = 6 \times 10^4/(\rho S_{BET})$. [c] Approximate number of crystallites per particle.

We start with presenting the factors that control the gas-phase synthesis and the impact they may have on the physical appearance and morphology of the nanocrystalline composite powders. Thereafter follows the results and discussion of the high-resolution TEM characterization, X-ray photoelectron spectroscopy, and high-energy diffraction, respectively.

3.1. Effect of the IGC-Synthesis Conditions. We have successfully produced samples that cover the whole compositional range (2−98% Cu). Previous research[17,27,32,47] has indicated that the most active catalyst composition for the oxidation of carbon monoxide into carbon dioxide is achieved for a composition range of 5−25% Cu on ceria. Therefore, this composition range was of special interest in this study.

The color of the oxidized composite varied with both copper content and particle size. With increasing copper content, the color changed from the pale yellow or white of cerium dioxide, over green-brownish to gray and dark black for the highest contents. Slight deviations from this color scale were observed if the particle size was altered, showing darker colors for smaller particle sizes. As the nanosized morphology is here shown to vary considerably, the surface composition may differ from that of the bulk composition, which has a large impact on the color of the powdered samples.[48] Noteworthy is here that the bulk composition of the CuO_x/CeO_2 powder samples is determined by energy-dispersive spectrometry (EDS), while the surface composition is evaluated by X-ray photoelectron spectroscopy (XPS). The resistant-heated crucibles were controlled amperometrically to achieve a constant vaporization rate. Two other parameters of special interest are the inert gas pressure inside the chamber and the geometrical configuration of the crucibles.

3.1.1. Helium Gas Pressure. The inert gas pressure during vaporization strongly affects the quenching probability of the metal clusters in their convective flux toward the coldfinger. It is widely known that with adjustment of the pressure of the inert gas, the particle size can be controlled.[9,11] The total gas pressure, which also could include reactive gases, for example, oxygen, affects the ease and the rate with which the metals are evaporated. Pressures in the range of 0.5−10 Torr He were tested. A too low pressure (<0.5 Torr) resulted in failed gas convection because of low quenching frequency of He atoms, while a too high pressure (>10 Torr) resulted in an uncontrolled heating and particle growth. A pressure of 1.0 Torr He was found to be the most favorable to produce a high BET surface area and to control the composition and size distribution of the Cu/Ce-metal clusters.

The ceria crystallite size increased significantly when the pressure was raised from 0.5 to 5 Torr. On the other hand, the secondary particle size (i.e., the cluster size of several agglomerated crystallites and amorphous material as determined form TEM measurements (D_{TEM})) appears to be more dependent on a helium pressure between 5 and 10 Torr (see Table 1). In Figure 3 a series of samples is shown that are produced at 1, 5, and 10 Torr helium pressure, respectively. (See further sections 3.2A and 3.4.2).

3.1.2. Vaporization Crucible Configuration. To our knowledge we are the first to use an adjustable multicrucible system to study the influence of the relative position of the crucibles upon the resulting nanosized morphology.[28] The phase diagram of metallic Cu and Ce[49] shows a series of intermetallic phases. However, it has been reported,[9−11] that the use of inert gas condensation cannot yield such intermetallic phases readily because of the high quenching rate observed during the thermalization process. As there is, to our knowledge, no ternary phase diagram of Cu−Ce−O available, one may assume that Cu has a very limited solubility in CeO_2.

Two- and three-crucible configurations were tested. The intention was to induce the formation of various interesting morphologies from a catalytic point of view, including core−shell particles. Figure 1a shows a photograph of one of the tested three-crucible configurations. A crucible that is filled with cerium is positioned in the center and confined by two copper-filled crucibles.

(47) Jiang, X.; Lu, G.; Zhou, R.; Mao, J.; Chen, Y.; Zheng, X. *Appl. Surf. Sci.* **2001**, *173*, 208.
(48) Mulvaney, P.; Liz-Marzán, L. M.; Giersig, M.; Ung, T. *J. Mater. Chem.* **2000**, *10*, 1259.
(49) Subramanian, P. R.; Laughlin, D. E. *Binary alloy phase diagrams*, 2nd ed.; Massalski, T. B., Ed.; ASM International: Materials Park, OH, 1990; Vol. 2, p 1051.

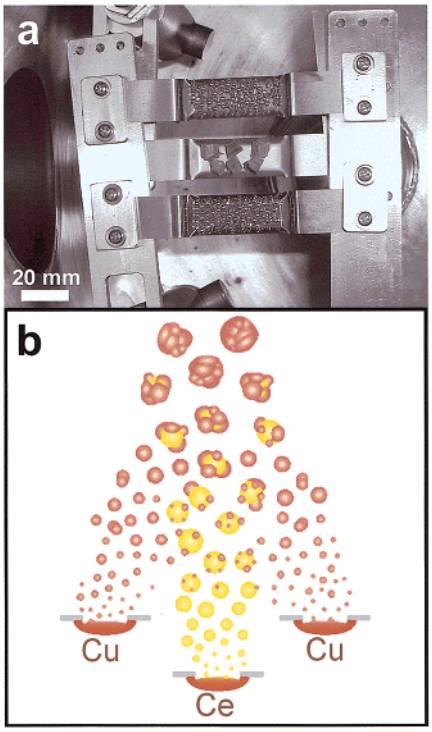

Figure 1. (a) Photograph of one of the tested three-crucible configurations. A Cu−Ce−Cu setup is shown. (b) Schematic illustration of the IGC quenching process of the Cu/Ce metal nanoclusters on their way to the cold collective finger. Note that the cluster sizes are exaggerated to illustrate the effect the crucible setup may have on the nanosized morphology.

A schematic drawing of the vaporization and quenching process illustrates how the metal clusters may be formed on their way toward the coldfinger (Figure 1b). Larger clusters with a broader size distribution are formed if the evaporated monomers are forced to travel a longer distance from the source.[50] Hence, with adjustment of the relative height and/or the distance between the two (or three) heating crucibles, the possibility to control the aggregation into particles was investigated. Our efforts to manipulate the nanosized morphology by alteration of the configuration of the crucibles turned out to be ineffective. We believe that the change in particle morphology is primarily a consequence of the copper content. Because shell structures (see Figures 9 and 10) are only observed for relatively high copper contents (30∼70%), this copper content level would provide the metallic Cu/Ce clusters optimal lattice expansion properties that would favor the formation of shells (such as rate of oxidation and volume increase) during the following oxygen treatment (see further section 3.2C). Hence, changes in the crucible configuration are considered to have a minor impact on the nanosized morphology because no obvious systematic correlation between the two parameters was observed. Nevertheless, by positioning the Cu crucible closer than the Ce-crucible to the collective coldfinger, we suggest that one can prevent the formation of larger bulk copper particles and provide for a higher copper dispersion after the oxygen treatment.

3.2. High-Resolution Electron Microscopy (HREM). Each IGC-produced sample shows a very specific morphology depending on its synthesis conditions and its copper content, but not crucible configuration. Powders with crystal sizes below approximately 1−2 nm do not exhibit detectable significant diffraction lines by X-ray powder diffraction and are known as "X-ray amorphous". Because of the amorphous character and the extreme dispersion of copper oxide on ceria, even the lateral resolution of high-resolution TEM is unable to accurately determine the copper distribution. These attributes making the characterization challenging are, however, suspected to be the main reasons for the known high catalytic activity of these samples.[21,23,32,38,39,46]

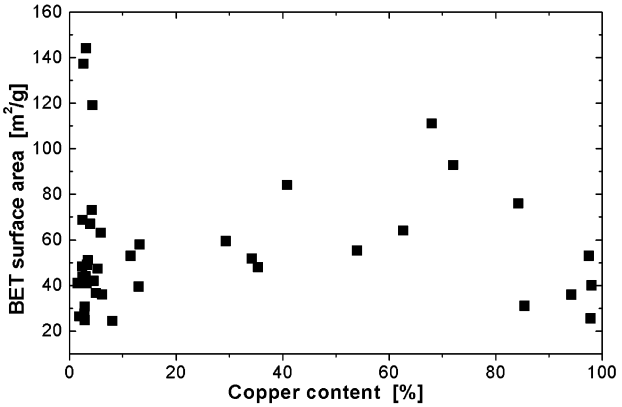

Figure 2. Plot of the BET surface area is independent of the copper content.

The specific surface area for all examined samples is shown to vary between 25 and 140 m^2/g, where a selection of the data is presented in Tables 1 and 2. In Figure 2, the specific BET surface area (S_{BET}) is plotted versus the copper content of the nanocrystalline CuO_x/CeO_2 samples. Because S_{BET} appears to be independent of the copper content, it is assumed that the S_{BET} is primarily influenced by the particle morphology.

On the basis of the results from XPS, HED, and previous catalytic results, the samples can be categorized into four compositional groups, A, B, C, and D, corresponding respectively to low (<6%), medium (6−25%), high (25−70%), and very high copper contents (>70%). The samples are referred in the text to their denoted name in Table 2, when that is possible.

Group A. Low Copper Contents (<6%). Typical electron micrographs (40 000×) of three samples (2.7(2)% Cu) produced at 1.0, 5.0 (A1), and 10.0 Torr He pressure, respectively, are shown in Figure 3a−c. The particle size is shown to increase from approximately 8 to 45 nm when the IGC chamber pressure was raised from 1 to 10 Torr (Table 1). As would be expected, the BET surface area diminished at the same time from 69 to 28 m^2/g.

It is worthwhile to calculate the mean BET surface area diameter (D_{BET}) for a spherical particle having an equivalent surface area, disregarding whether the particle consists of one single crystallite or several crystallites. The D_{BET} sizes are always larger than the crystallite size obtained from Scherrer peak-broadening analyses (D_β), which suggests that the crystallites are agglomerated to form particles or enveloped by amorphous material. The average number of crystallites contributing to a particle is equal to the ratio of $\langle D_{BET}/D_\beta \rangle^3$ (see section 3.4.2). As would be expected, the

(50) Uyeda, R. *J. Cryst. Growth* **1974**, *24*, 69.

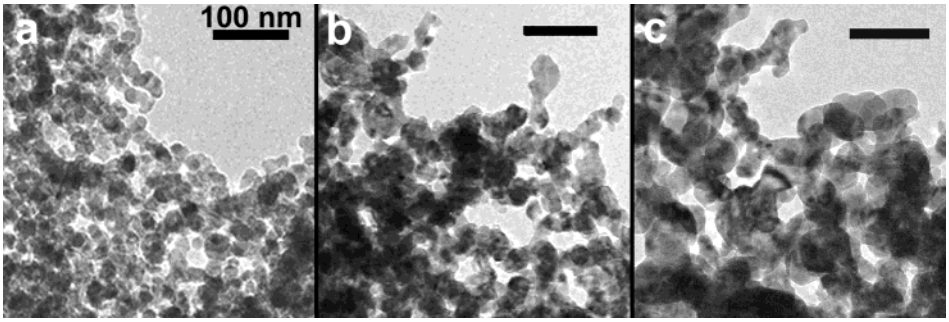

Figure 3. Electron micrographs displaying nanoparticles of the CuO_x/CeO_2 nanocomposite (2.7 ± 0.2% Cu) produced at various helium pressures: (a) 1.0 Torr, (b) 5.0 Torr, and (c) 10 Torr.

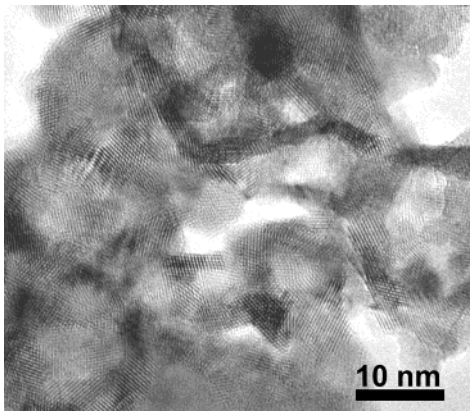

Figure 4. High-resolution electron micrograph showing nanocrystallites of CeO_2 seemingly forming tangled shells (4.2% Cu).

calculated values of D_{BET} size agree well with the particle sizes determined from the transmission electron micrographs (D_{TEM}) (Table 2). However, an accurate estimate of the crystallite size by HREM in such materials is associated with significant statistical errors.

Samples with low copper contents, such as those shown in Figures 3−5, generally exhibit small ceria crystallites embedded in a thin amorphous layer, but with no traces of crystalline CuO_x. A few samples (around 4.2% Cu), which had little or no amorphous material, showed a morphology with tangled shells (Figure 4). At these very low copper contents (<4%), the probability is high for an encapsulation (or decoration) of the copper species by crystalline CeO_2, which thereby would make it inaccessible for, for example, CO adsorption.[26,51]

With a copper content just below 5% we find a sample showing smoothly interfaced particles with typical rounded shapes (A4, Figure 5). At lower magnifications (120 000×) the sample is consisting seemingly of very poorly crystalline material, judging from the rounded particle shapes (Figure 5a) and from the continuous rings in the corresponding selected area diffraction (SAD) pattern (Figure 5b). At higher magnifications, however, the composite particles are revealed to be assembled by randomly oriented and epitaxially interfaced crystallites (Figure 5c). The most frequently observed crystal lattice planes of CeO_2 are indicated in the figure (d_{111}(3.13 Å); d_{200}(2.71 Å); d_{220}(1.91 Å)). The high presence of Moiré fringes may be taken as an indication of aggregates consisting of epitaxially interfaced nanocrystallites, which gives a higher degree of X-ray amorphicity (incoherent scattering) in HED. In fact, the lowest X-ray crystallinity (see further section 3.4.3) was obtained for this sample, that is, showing poorly crystalline character at low magnification.

Group B. Medium Copper Content (6−25%). For copper concentrations between 6 and 25%, the composite catalyst exhibits representatively a uniform morphology with a narrow particle size distribution. In Figure 6a,b the sample B4 (13.1% Cu) is shown. Displayed at higher magnification, the apparently solid matrix is shown to consist of tightly interfaced crystallites. Even for these relatively high copper contents, no distinct proof of crystalline copper, or copper oxide, could be observed by electron microscopy or selected area electron diffraction. This is corroborated by high-energy diffraction, where no diffraction lines from copper could be detected. Because this composition range is known for exhibiting the best catalytic activity for CO oxidation, the HREM images were scrutinized by FFT analysis and indications of lattice spacing in the range 2.0−2.6 Å were found. This could be significant for CuO_x crystallites that are "sandwiched" between the ceria crystals (Figure 6b, inset). For a sample with 6.1% Cu (Figure 7), small apparently amorphous surface clusters, possibly CuO_x, were found evenly distributed on top of ceria crystals. Such clusters would provide excellent adsorption sites for reactant molecules, but as they are here easily detected (≈1 nm), we believe that these are unnecessarily large for a catalytic process.[32]

In Figure 8 are shown electron micrographs of sample B1 (6.1% Cu), which exhibits a high number of block-shaped particles having sharp, facetted edges and flat surfaces. The high-resolution micrograph in Figure 8b clearly shows larger single crystals, which expose a high portion of low-energy surfaces in the absence of amorphous material. These features are more commonly found in samples with higher X-ray crystallinity (see further section 3.4.3). We suggest that a high X-ray crystallinity of the ceria phase contributes to lower copper dispersion, giving rise to the relatively large surface clusters of CuO_x that can be resolved by HREM (Figure 7).

Group C. High Copper Contents (25−70%). As the copper content is increased above 25%, the composite catalyst shows a tendency to form crust structures. Figure 9 displays a representative sample with 29% Cu (C1) where the cerium dioxide nanocrystals form elongated shell structures with an apparently empty core. A zero-loss image of the C1 sample with the complementary EFTEM element maps of Ce, Cu, and O,

(51) Benaïssa, M.; Pham-Huu, C.; Werckmann, J.; Crouzet, C., Ledoux, M. J. *Catal. Today* **1995**, *23*, 283.

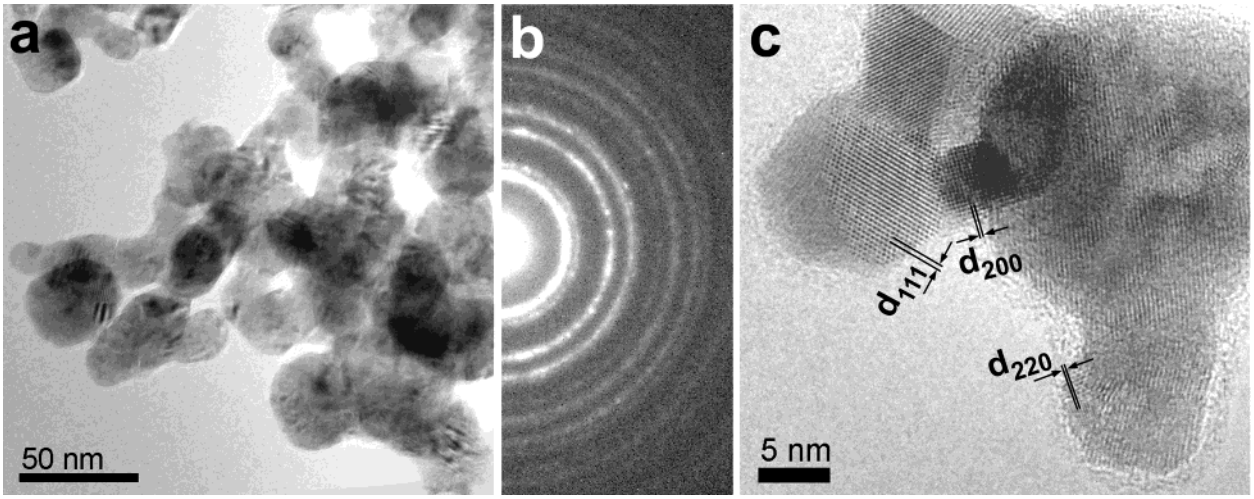

Figure 5. This sample (A4; 4.9%Cu) displays exceptionally rounded particle shapes exhibiting the lowest crystallinity factor (section 3.4.3). (a) Viewed at lower magnifications, the smoothly aggregated particles seem amorphous, showing a characteristic high contrast caused by the numerous Moiré patterns. (b) The corresponding SAD pattern with the continuous rings of CeO_2. (c) The particles are shown to consist of randomly oriented and epitaxially interfaced nanosized crystallites. The three most commonly found *d*-spacings are indicated.

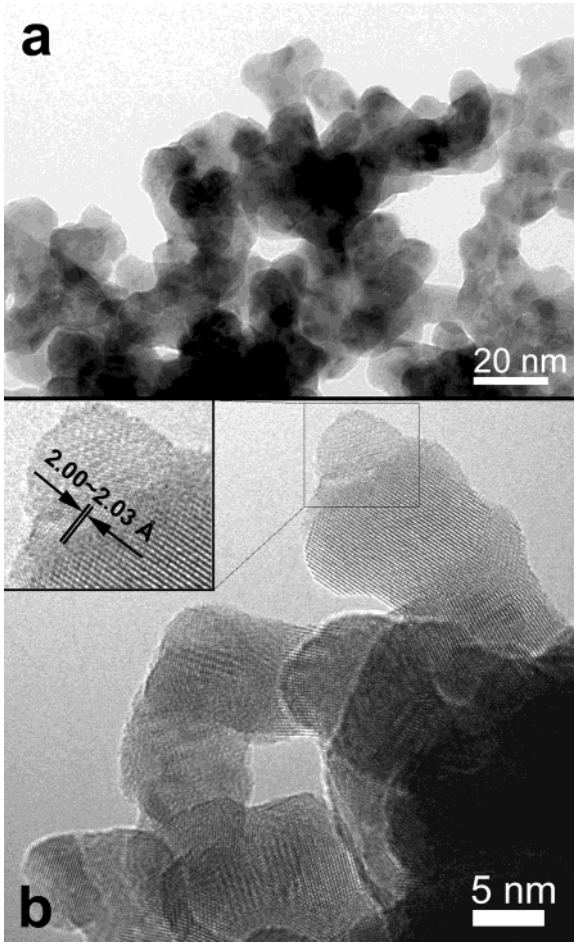

Figure 6. (a) At medium copper contents (Group B) the composite morphology appears as an amorphous solid matrix (sample B4; 13.1% Cu). (b) At higher magnification the particles are revealed to consist of tightly interfaced CeO_2 crystallites. Traces of what could be crystalline Cu/CuO_x were occasionally found. The inset shows possibly a trace of squeezed metallic Cu crystallite.

respectively, is shown in Figure 9c (FEG-TEM Technai 300 kV, GIF). Even at this high magnification (400 kX) the copper seems evenly distributed over the ceria

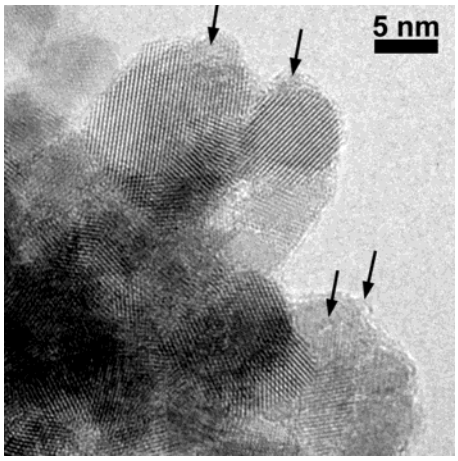

Figure 7. High-resolution TEM image of a sample (B1; 6.1% Cu) showing CeO_2 crystallites embedded in thin amorphous film. The arrows point to some amorphous subnanosized clusters that could be superficial X-ray amorphous crystalline copper oxide.

lattice, with no signs of a complementarity to the Ce map, which confirms an extremely high dispersion. A core−shell structure with an apparently empty core is shown in Figure 10b. This is an electron micrograph of the same sample shown in Figure 10a, but after it has been stored in ambient air for several months. Notably, the shell morphology is preserved by a stable structure of cerium dioxide that prevents it from collapsing.

When cerium metal is oxidized to cerium dioxide, the lattice volume expands by approximately 41% (a_0(Ce) = 4.82 Å, $a_0(CeO_2)$ = 5.41 Å). In pure oxygen the oxidation rate of cerium metal is very high, which causes cerium oxide to immediately form a thin layer. A continued growth of the oxide layer will force cerium ions to migrate outward through the oxide surface layer, which would lead to a depletion of the core. As crust structures are only observed for relatively high concentrations of copper (30∼70%), we postulate that this is the main reason for allowing crust structures to form. Assuming that the metallic clusters of Ce and Cu prior to oxidation are well mixed, the high portion of copper

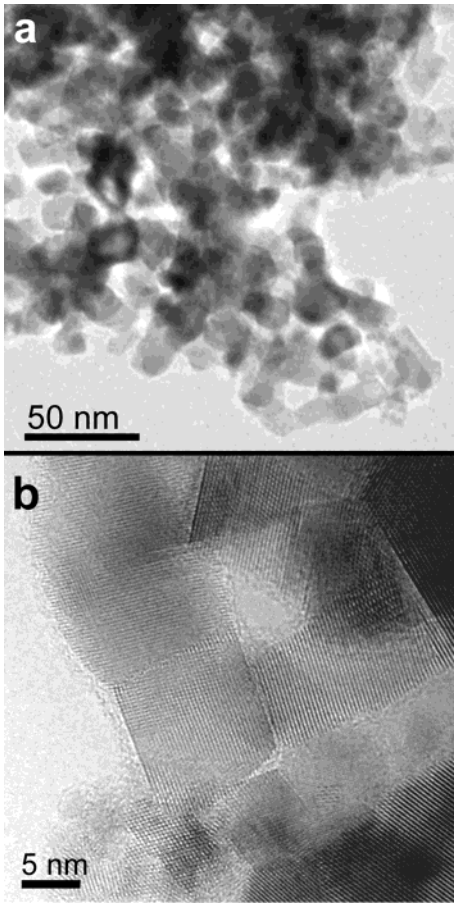

Figure 8. (a) Low-magnification TEM micrograph of a relatively highly crystalline sample (B1; 6.1% Cu) displaying larger block-shaped particles and sharp edges. (b) At high magnification the crystalline CeO_2 octahedra are shown to expose predominantly (111) surfaces.

would give the clusters optimal lattice expansion properties (such as oxidation rate and volume increase) during the following oxygen treatment. We have constructed a scheme in three consecutive steps shown in Figure 11 to illustrate the growth mechanisms of shell structures described above. The considerably higher free energy of the oxidation ($\approx 7\times$) of cerium metal, compared to that of copper metal ($-\Delta G_f°(CeO_2) > -\Delta G_f°(CuO)$),[52] would facilitate a migration of the cerium ions toward the surface of the Cu/Ce-metal cluster, forming a nanocrystalline cerium oxide shell. The copper-enriched metal left inside migrates along the boundaries of the cerium oxide nanocrystallites and will be oxidized by oxygen coming from the CeO_2 lattice. This could explain the exceptionally high dispersion of copper on ceria because the copper does not form isolated crystallites nor cause a significant contraction of the cerium dioxide lattice (sections 3.4.1 and 3.4.2).

Additional chemical imaging using energy-filtered TEM (LaB_6-TEM, Philips CM120, GIF) at lower magnifications further confirmed that the copper is indeed well dispersed over the ceria support. Figure 12 shows EFTEM maps of a sample with 54% (C2) copper. For copper contents above approximately 30%, diffraction lines of a CuO phase start to appear in HED. However, for samples with copper contents between 30 and 70%, traces of larger tenorite CuO particles could not be detected by EFTEM or by high-resolution TEM. In Figures 9c and 12, a substantial portion of the Cu appears to remain highly dispersed in the sample even above a 30% copper content. Hence, our IGC-produced samples may thereby exhibit a copper dispersion similar to that of the samples presented earlier by Ying and co-workers[9,10,53] and Liu and Flytzani-Stephanopoulos.[17] Consistent with the results obtained by HED, the portion of copper in the Cu maps does not appear to represent the total amount of copper in these specific samples, which would indicate that the crystalline copper phase is agglomerated into larger aggregates or embedded in thick amorphous material. Such particles would prevent lattice imaging of individual copper oxide phases.

For a sample with 68% copper (C3), displayed in Figure 13, the observed ceria crystallites appear to be rounded and less frequently aggregated into larger particles. Evidently, this gives high BET surface area and a low $\langle D_{BET}/D_\beta \rangle^3$ number (i.e., the crystallites are less aggregated into larger particles (Table 2)). Even for this high copper content fast Fourier transform (FFT) analyses of micrographs show only lattice spacing of CeO_2 and do not reveal patterns from crystalline copper or copper oxides (Figure 13, inset).

Group D. Very High Copper Contents (>70%). Samples with very high copper contents show an amorphous character with smoothly interfaced particles. The few ceria crystallites that could be found were either well embedded in an amorphous copper oxide matrix or evenly distributed on top as capping islands (Figure 14). For the latter case, the copper matrix displays a crystalline core enveloped by amorphous copper oxide, which acts as a support for the nanosized crystalline ceria caps. In samples consisting of more than 95% copper, crystals of Cu and Cu_2O were easily found, while CuO (tenorite) occurred less frequently.

3.3. X-ray Photoelectron Spectroscopy (XPS). *3.3.1. Dispersion Capacity.* It is known that the distribution of the copper species is influenced by the support material, but can also be strongly influenced by the preparation method.[26] Catalysts produced, for example, by the impregnation methods or by ion exchange, normally exhibit a maximum dispersion capacity of active metal on high surface area supports.[26,54,55] Incorporation models have been used to predict the maximum dispersion by taking into consideration both the surface structure of the support and the valency of the supported species.[56] Dong et al.[55,57] have shown that the maximum dispersion capacity of CuO on CeO_2 for impregnated samples (12 μmol/m^2) corresponds well to such model predictions. A loading above the maximum dispersion capacity results in the appearance of bulk CuO as shown by XRD. We have plotted in Figure 15a the XPS peak intensity ratio of I_{Cu}/I_{Ce} (analysis depth

(52) Weast, R. C. *CRC Handbook of Chemistry and Physics*; CRC Press Inc.: Boca Raton, FL, 1985.

(53) Tschöpe, A.; Ying, J. Y.; Chiang, Y.-M. *Mater. Sci. Eng. A* **1995**, *204*, 267.
(54) Hu, Y.; Dong, L.; Wang, J.; Ding, W.; Chen, Y. *J. Mol. Catal. A* **2000**, *162*, 307.
(55) Dong, L.; Jin, Y.; Chen, Y. *Sci. China B* **1997**, *40*, 24.
(56) Chen, Y.; Zhang, L. *Catal. Lett.* **1992**, *12*, 51.
(57) Dong, L.; Hu, Y.; Xu, F.; Lu, D.; Xu, B.; Hu, Z.; Chen, Y. *J. Phys. Chem. B* **2000**, *104*, 78.

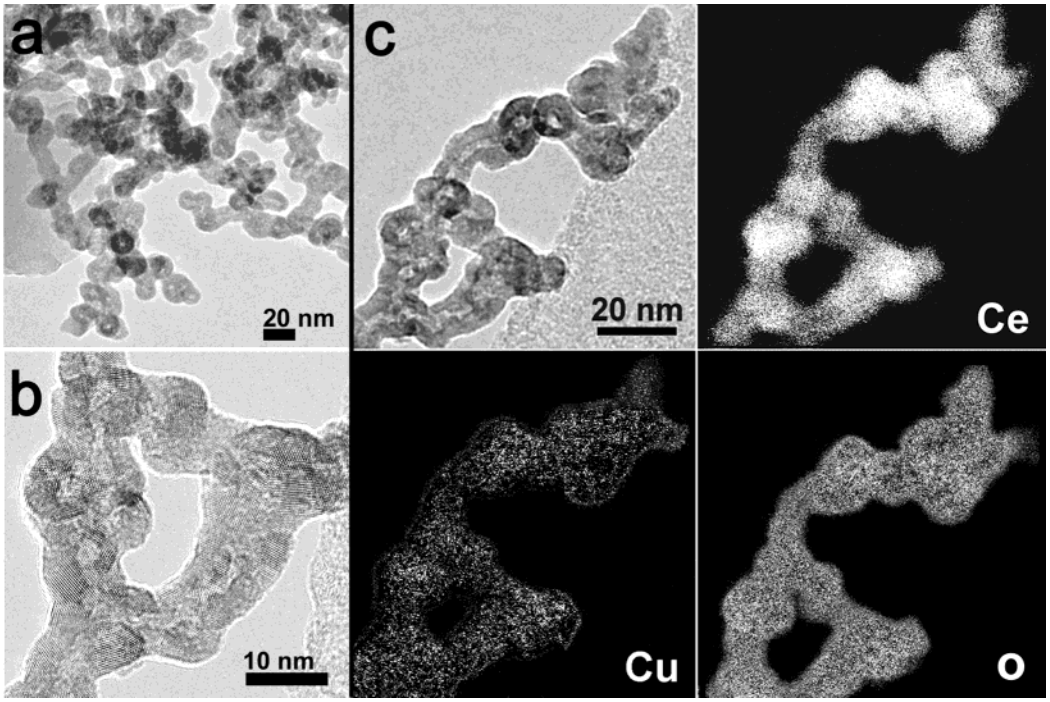

Figure 9. For copper contents between 30 and 70%, many samples exhibit various crust structures. (a) A sample with 29% Cu (C1) displaying an elongated shell structure with an apparently empty core. (b) High-magnification image showing the many tightly interfaced CeO_2 nanocrystals. (c) Zero-loss image of the same area together with the corresponding high-resolution energy-filtered TEM elemental maps of Ce, Cu, and O.

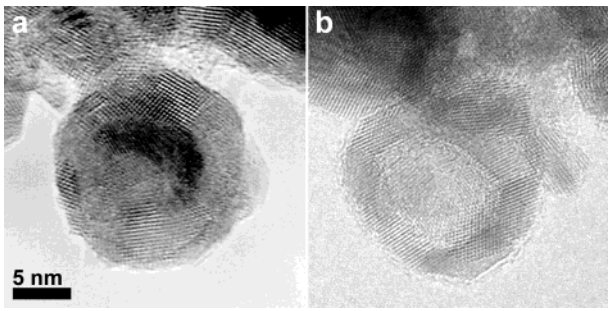

Figure 10. A high number of core−shell structures were found in the sample shown here (63% Cu). (a) HREM micrograph of the freshly prepared sample still displayed a dark metallic core. (b) Image from the same sample, but after storage in air for several months. The core−shells exhibit an apparently empty core. (*Note that the images display two different particles*.)

<2 nm) as a function of the bulk copper content (as determined by XEDS). (Only principal peaks, the Cu(II) $2p_{3/2}$ and Ce(IV) $3d_{3/2}$, respectively, were integrated to avoid the variations in the degree of reduction). This represents a quantitative evaluation of the dispersion properties of the copper species at the ceria surface. We observe a steady increase of the I_{Cu}/I_{Ce} ratio over the whole compositional range, which indicates no apparent maximum dispersion limit of copper over ceria. The crystal growth in gas-phase synthesis is therefore exceptional in the respect that it can provide high surface dispersion at high copper concentrations, even after bulk CuO starts to appear at approximately 30% Cu (section 3.4.1). (Similar results have also been reported for coprecipitated[17,58,59] or sol−gel-prepared[23] Cu/Ce/O catalysts). At a loading of 30% Cu, the copper oxide that is exposed on the surface corresponds to almost 6-fold higher maximum dispersion capacity per square meter of catalyst area, when compared to what is observed and predicted for an impregnated catalyst.[55]

At copper contents between 5 and 15%, the dispersion of surface copper appears to deviate and exhibit higher values than expected from the bulk composition (Figure 15a). Hence, a larger amount of surface copper is available and presents a higher density of adsorption sites for the reactant gases. On the other hand, a significant surface discrimination for higher copper contents can be noted in Figure 15a. This is interesting to note as several of the IGC-produced samples with 30∼70% Cu actually display crust structures (Figures 9 and 10). The formation of crust structures, as discussed above and illustrated in Figure 11 (section 3.2C), may be due to a sequential oxidation of Ce followed by Cu, which would leave the major portion of copper species highly dispersed or encapsulated inside the CeO_2 polycrystalline aggregates. By minimizing the total amount of surface area exposed, and predominantly exposed surfaces of low surface energy, the total surface energy would be reduced. However, in principle, thermodynamic equilibrium conditions should prevail. The CeO_2(111) surface exhibits the lowest surface energy,[5,15] indicating that this surface would be the most frequently exposed surface.[60,61] This was indeed also detected by HED, showing a higher portion of (111) surfaces (section 3.4.2). If the surface energy of CeO_2(111) is significantly lower than that of any of the copper oxides, the result would theoretically be an encapsulation of the copper species

(58) Kundakovic, Lj.; Flytzani-Stephanopoulos, M. *Appl. Catal. A* **1998**, *171*, 13.

(59) Lamonier, C.; Bennani, A.; D'Huysser, A.; Aboukaïs, A.; Wrobel, G. *J. Chem. Soc., Faraday Trans.* **1996**, *92*, 131.

(60) Jacobsen, S. N.; Helmersson, U.; Erlandsson R.; Wallenberg, L. R.; Skårman, B. *Surf. Sci.* **1999**, *429*, 22.

(61) Kuo L.-Y.; Shen P. *Mater. Sci. Eng. A* **2000**, *277*, 258.

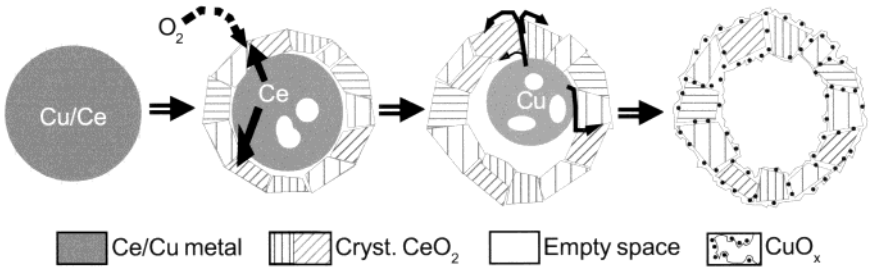

Figure 11. This scheme, in four consecutive steps, may illustrate the growth mechanism for the observed crust structures between 30 and 70% Cu. A sequential oxidation of Ce followed by Cu and an ideal proportion of lattice expansion may explain the exceptionally high copper dispersion on ceria as well as the formation of such stable morphologies.

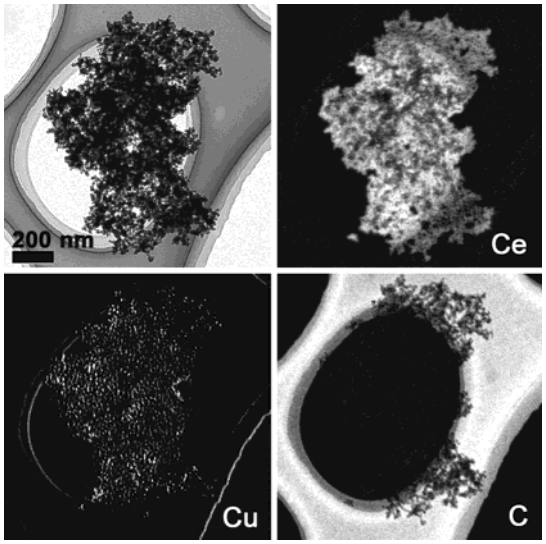

Figure 12. Low-magnification elemental maps of Ce, Cu, and C, respectively, as recorded by GIF-EFTEM on sample C2 (54% Cu). The CuO_x/CeO_2 composite particle aggregates, still showing no signs of larger bulk CuO particles, are dispersed on a holey-carbon grid, which is clearly detected in the carbon map.

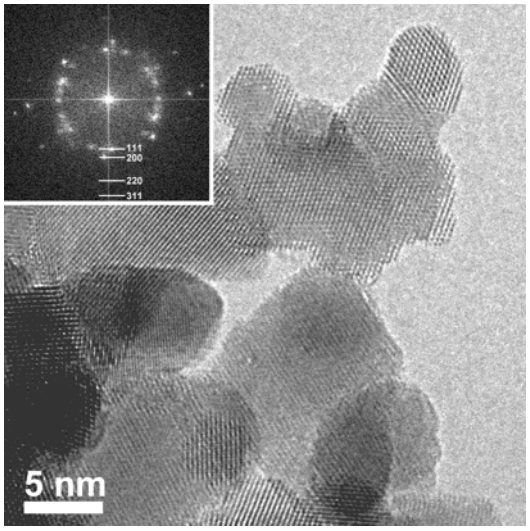

Figure 13. HREM micrograph of a sample (C3; 68% Cu) with the highest specific surface area shows exceptionally spherical CeO_2 crystals, which are less aggregated into larger particles. Even for this relatively high copper content, signs of a crystalline Cu/CuO_x phase were not found by SAED, HREM, or FFT-image analysis (inset).

or clusters by the cerium dioxide. Surface discrimination of copper may also be augmented if the highly dispersed copper clusters are located predominantly at the boundaries of the CeO_2 crystallites, which would result in a proportionally lower surface copper concentration for increasing copper contents because the area of internal crystal boundaries always are larger than the exposed surface area of the aggregate.

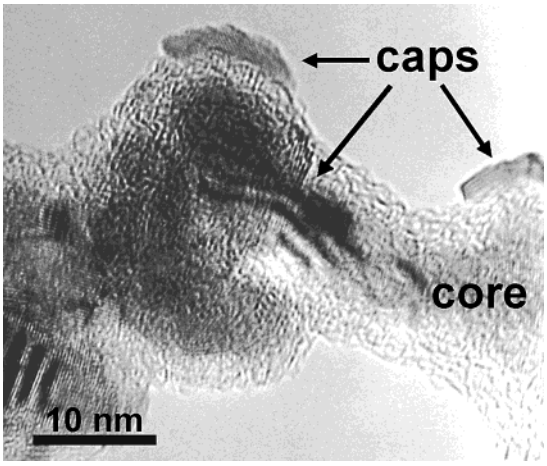

Figure 14. The very high copper content (98%) in this sample resulted in an amorphous copper oxide matrix having a crystalline core. Crystalline CeO_2 caps were found evenly distributed on top, which give rise to Moiré patterns.

3.3.2. Surface Valency. For Cu-containing compounds, the intensity of the satellite peaks (at ≈943 and ≈963 eV binding energy) decreases with the reduction of Cu^{2+} because the d shell of both Cu^0 and Cu^{1+} are filled and, therefore, cannot give rise to satellite peaks.[62−64] Thus, the degree of reduction can be investigated by determining the ratio of intensities of the satellite peaks to those of the principal peaks (I_{sat}/I_{pp}) (Figure 15b). A lower ratio, compared to our Cu(II) reference sample (at 0.57, dotted horizontal line in Figure 15b),[55,63] would thus indicate reduced surface copper states. However, the determination of the valency of copper is a well-known problem. Because copper is easily reduced during exposure to electrons (EELS) or photons (XPS),[17,37,38] the analysis time in the XPS measurements must be as short as possible, and consequently, a poor signal intensity and statistical confidence results. Indications of reduced surface states are nevertheless noticeable in Figure 15b. Preliminary results performed by EXAFS measurements also confirm a minor presence of Cu(I) species in as-prepared samples.[32]

(62) Chusuei, C. C.; Brookshier, M. A.; Goodman, D. W. *Langmuir* **1999**, *15*, 2806.
(63) Frost, D. C.; Ishitani, A.; McDowell, C. A. *Mol. Phys.* **1972**, *24*, 861.
(64) Evans, S. *J. Chem. Soc., Faraday Trans. 2* **1975**, *71*, 1044.

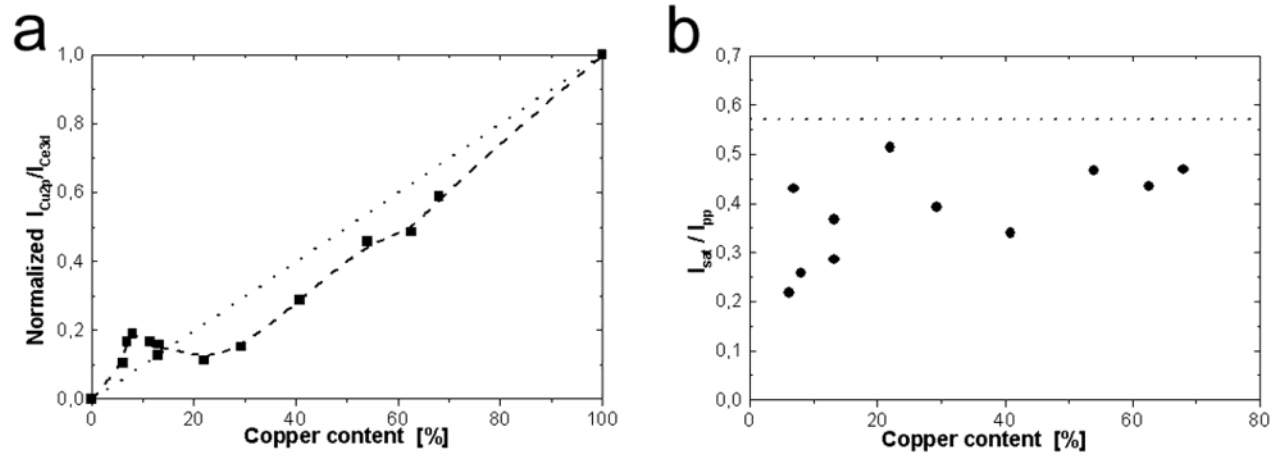

Figure 15. Evolution of XPS characteristics of the CuO_x/CeO_2 composite with the bulk copper content. (a) Indicating the predominant location of surface copper (<2-nm depth). The dotted diagonal line represents the calculated copper content of the surface according to the bulk concentration. (The peak intensity ratio has been normalized to reference samples of CeO_2 and CuO, for which the ratio is set to be 0 and 1, respectively.) (b) Showing the reduction degree of surface copper. The dotted horizontal line represents the ratio for a Cu^{2+} reference sample (CuO).

According to Shyu et al.,[65] the fraction of the Ce(IV) $3d_{3/2}$ peak (at ≈916.8 eV) to the total Ce 3d intensity depends on the Ce^{3+}/Ce^{4+} ratio. A slightly reduced CeO_2 surface is confirmed by a decreased ratio as well as a shift of the Ce(III) $3d_{5/2}$ (at ≈882.6 eV) to higher binding energies[32] (see further section 3.4.2).

3.4. High-Energy Diffraction (HED). *3.4.1. Detectable Phases.* High-energy X-ray diffraction patterns of some of the CuO_x/CeO_2 catalysts are presented as a function of the 2θ scattering angles in Figure 16a,b. The diffractograms that are selected for presentation are chosen not only to suitably illustrate the variations in peak width (i.e., proportional to the crystal size) and background intensity but also to show the detection limit of bulk CuO (tenorite). The acquisition time, corresponding to an equivalent sample quantity, was identical for all the samples.

The main peaks located at $\beta_{2\theta} \approx 2.54°$, 4.15°, and 4.87° (corresponding to the *d* values of 0.313, 0.191, and 0.163 nm) could be indexed respectively with the reflections (111), (220), and (311) of the face-centered cubic fluorite phase of CeO_2 (space group $Fm3m$). For copper contents higher than 30%, peaks characteristic of the CuO crystalline phase at $\beta_{2\theta} = 3.14°$ and 3.42° begin to appear (Figure 16b and inset). Thus, below 30% Cu the copper appears to be X-ray amorphous and highly dispersed. This finding is supported by others, also using IGC synthesis,[9] but is shown to be formed at much lower concentrations if coprecipitation,[17,23,58] sol−gel,[22] or impregnation syntheses[47] are utilized. However, one should keep in mind that the small crystallite size of CeO_2 gives rise to very broad and poorly resolved peaks, which makes the detection of minor amounts of crystalline copper oxides difficult. Upon calcinations at 684 K and above, previous results have shown that highly dispersed copper ions begin to segregate and form bulk CuO, but with a substantial fraction of copper remaining highly dispersed within the ceria clusters or on their surfaces.[9,10,53] In some cases it has been reported[17,23] that the originally small detectable quantity of crystalline CuO phase disappears by heating to 873 K and is still not detected at 981 K. The authors[23] suggest that the CuO phase upon heating is transformed into finely dispersed clusters (X-ray amorphous) lying on the surface of larger CeO_2 crystallites. We discuss this phenomenon together with our XAFS results in more detail elsewhere.[32]

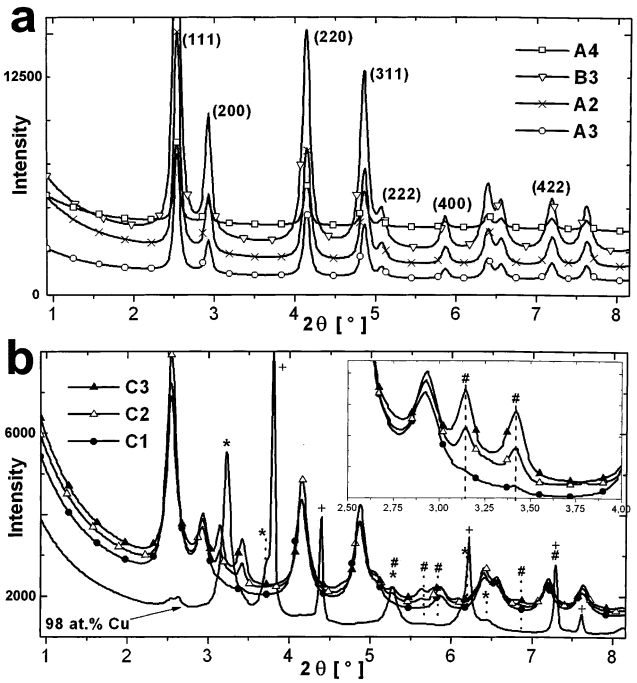

Figure 16. High-energy diffraction patterns of the CuO_x/CeO_2 composite with increasing copper contents (see Table 2 for notation). (a) The major reflections of the fcc fluorite CeO_2 phase are indicated. (b) Diffractograms of samples with high copper contents. The major peak reflections from Cu (+), Cu_2O (*), and CuO (#) are indicated. Note that for 29% Cu (C1) the characteristic peaks of CuO begin to appear (inset zoom). The lower black diffractogram represents a sample with 98% copper content.

For the samples exhibiting diffraction peaks of the copper phases, it appears as if there is no systematic correlation to the total copper content. Thus, we may conclude that the copper remains highly dispersed even

(65) Shyu, J. Z.; Weber, W. H.; Gandhi, H. S. *J. Phys. Chem.* **1988**, *92*, 4964.

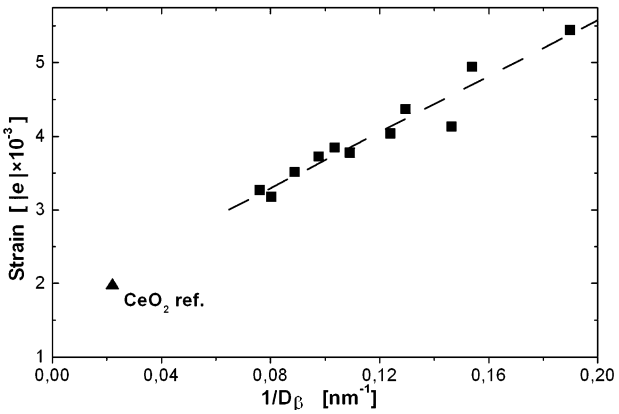

Figure 17. The reciprocal crystal size by Scherrer versus the rms strain. The rms strain is shown to increase continuously with decreasing CeO_2 crystal size.

after additional bulk copper oxide phases have been formed. This is in good agreement with the results reported by Ying and co-workers[9,10,53] and others.[17,47,66]

For copper contents between 30 and 95% (~Group C) the only copper oxide phase detectable by X-rays is the black tenorite CuO (Figure 17b). Reduced phases (Cu and Cu_2O) are only detected above a 95% copper content (Figure 16b). Normally, when copper is oxidized in air, it stabilizes under the Cu_2O form.[52] This suggests that the cerium dioxide lattice can contribute to the oxidation of initially formed Cu_2O clusters into fully oxidized CuO effectively. However, if the copper content is too high (>97%), the small quantity of cerium dioxide can no longer sustain the oxidation of the copper phase, and larger crystals of reduced phases, such as Cu metal or Cu_2O, will emerge.

3.4.2. Peak Broadening and Variations in the Unit Cell Parameter. Relative to the microcrystalline CeO_2 reference sample (cell parameter $a_0 = 0.5415$ nm) the peaks of the samples produced in the gas phase display an averaged negative angular diffraction shift of $\beta_{2\theta} = -3.51 \times 10^{-3}$ °, indicating a unit cell expansion (ca. 0.08 vol %) and the presence of a slightly reduced fcc ceria phase ($CeO_{2-\delta}$). This was confirmed by the XPS measurements (section 3.3.2). The cell parameters of some representative samples in the composition range 2−68% Cu are summarized in Table 2. An ordered reduction of the cerium dioxide would cause an expansion of the unit cell (closer to CeO_{2-x} or the *C*-type sesquioxide Ce_2O_3[4,23,67,68]). It is known that nanocrystalline ceria synthesized by IGC,[9] or size-fractionated sols of ceria nanocrystallites,[69] can present a lattice expansion because of reduction even at room temperature. An enhanced reducibility of the nanocrystalline Cu-doped ceria has been clearly demonstrated.[70] However, a simultaneous inclusion of copper ions and ordered removal of oxygen would, at least partly, be canceled by the contraction of the lattice because of the replacement of Ce ions by the smaller Cu ones and, thus, eliminate the possibility to quantify this effect by HED.

The average size of the CeO_2 nanocrystallites was calculated according to the Scherrer equation. The growth of low-energy surfaces is favored, which can be observed in the HED pattern of CeO_2 by comparing the peak width for some major diffraction lines. The crystal size parallel to the (111) lattice planes measured slightly larger crystal sizes (+9.3%), that is, flat crystals, truncated by {111} surfaces. Hence, the CeO_2(111)-type surface is more commonly exposed than the other low indexed surfaces. Therefore, the mean crystal size (D_β) was taken as the average value from four of the main diffraction peaks of CeO_2 and presented in Tables 1 and 2. The He pressure during the IGC synthesis was shown to control both the crystal size and the particle size.

The IGC-produced as-prepared samples exhibit small diffraction line variations ($\beta_{2\theta}$) amounting to $a_0 = 0.54183(37)$ nm. The angular deviations show, as expected, no obvious systematic correlation to the crystallite size. Thus, the crystals in our sample series are too large to show a lattice expansion because of surface relaxations.[69] For increasing copper contents, a weak positive correlation can be noted, which would indicate a diminutive contraction of the unit cell because of the incorporation of copper ions. However, the rms strain is shown to increase continuously for decreasing crystal sizes (D_β). In Figure 17 the reciprocal Scherrer crystal size ($1/D_\beta$) is plotted versus the root-mean-square strain. If the unit cell parameter is normalized for the strain contribution, the apparent contraction for increasing copper contents is eliminated. Hence, the observed angular deviations in the HED patterns cannot be an indication of a lattice contraction of the nanocrystallites because of the incorporation of copper ions. Neither can it be a consequence of reduction, which would show an increased lattice expansion for decreasing crystal sizes. The detected averaged angular deviations are therefore apart from instrumental noise, expected to be an effect of variations in the rms strain only.

3.4.3. Crystallinity Factor. We have determined the crystallinity in close accordance with the work by Hermans and Weidinger.[71] The total peak area I_P (collected in the range $0.923° < \beta_{2\theta} < 8.158°$), which is set to represent the coherent radiation diffracted selectively by the crystalline portion of the sample, is integrated using a least-squares fit of a Gaussian function over a manually fitted baseline. The background intensity I_B is defined as the area between the $I = 0$ line and the manually fitted baseline. The I_B may, thus, be taken as a relative measure of the disordered fraction of the sample (i.e., the fraction of noncrystalline material and the very small crystallites undetectable to X-rays). A *crystallinity factor* can then be defined as the ratio I_P/I_B given in Table 2. Because a ratio is used for comparison, we assume that the generally insignificant incoherent radiation and scattering from air and the sample holder are eliminated. It is assumed that when the I_B value approaches zero (i.e., giving higher I_P/I_B ratios), the sample consists entirely of highly crystalline material. As the I_P value represents the total crystalline portion, no consideration is taken to distin-

(66) Daniell, W.; Lloyd, N. C.; Bailey, C.; Harrison, P. G. *J. Phys. IV* **1997**, *7*, 963.
(67) Vasiliu, F.; Parvulescu, V.; Sarbu, C. *J. Mater. Sci.* **1994**, *29*, 2095.
(68) Perrichon, V.; Laachir, A.; Bergeret, G.; Fréty, R.; Tournayan, L.; Touret, O. *J. Chem. Soc., Faraday Trans.* **1994**, *90*, 773.
(69) Tsunekawa, S.; Sivamohan, R.; Ito, S.; Kasuya, A.; Fukuda, T. *Nanostruct. Mater.* **1999**, *11*, 141.
(70) Tschöpe, A.; Ying, J. Y.; Amonlirdviman, K.; Trudeau, M. L. *Mater. Res. Soc. Symp. Proc.* **1994**, *351*, 251.
(71) Hermans, P. H.; Weidinger, A. *J. Polym. Sci.* **1949**, *4*, 135.

guish the relative portion of different crystalline phases in the sample. Despite the inherent inapplicability of the terms *crystalline* and *amorphous* to metal oxides, there is an undoubted utility in employing the terms for empirically categorizing a given sample relative to others on an arbitrary (and quantitatively uncertain) numerical scale of ordering. Thus, the results must strictly be used for comparison between samples of the same materials within a similar series of experiments and preferably evaluated in connection to the results obtained by TEM. The semiquantificational error in categorizing crystallinity of CeO_2 by X-ray diffraction has been estimated to approximately ±20%.[72] However, the confidence in the results is improved by the use of high-energy synchrotron radiation.[40]

As copper oxide, compared to CeO_2, shows[52] lower propensity to form long-range ordered crystalline material, especially when it is produced in the gas phase,[9,25,46] it is expected that the defined crystallinity factor would decrease with increasing copper content. However, no significant systematic correlation was found between the I_P/I_B ratio and the copper content, neither to the crystal size of CeO_2. A stronger X-ray absorption background (diffuse scattering), for example, the one observed for sample A4, would normally be classified as a water adsorption effect:[36] Dependent on the nanosized morphology and the portion of differently exposed crystallographic surfaces, the sample may adsorb more or less water or hydroxyl groups.[46] Therefore, we scrutinized FT-IR spectra over the typical vibration frequency known for adsorbed water and hydroxyl groups (2800−3700 cm^{-1}),[73] but the enhanced background level in HED could not be explained by such adsorbed species. Moreover, the transmission electron microscopy investigation showed no obvious indications of amorphous material that could account for the whole measured difference in the crystallinity factor. Instead, by a careful HREM examination, we found a clear morphological connection to the I_P/I_B ratio: For similar copper contents, rounded particles shapes formed by epitaxially interfaced crystallites occurs more frequently in samples with lower crystallinity factor (Figure 5), while block-shape particles exhibiting sharp edges and distinct flat surfaces are more common in samples presenting a higher crystallinity factor (Figure 8 and section 3.2A). A particle that exhibits smoothly rounded shapes, such as sample A4, exposes preferentially a larger portion of crystallographic steps and edges forming various high-energy facets (Figure 5). Hence, we suggest that this kind of nanosized morphology inherits a higher portion of X-ray invisible material (sample specific incoherent scattering), which would enhance the background intensity in HED.

If the sample crystallinity is high, the particle diameter evaluated by TEM (D_{TEM}) is shown to be in closer accordance with the mean Scherrer crystal size (D_β), determined by HED (Tables 1 and 2). A D_{TEM} similar to D_β also indicates that there are less crystallites per particle (see Figure 13). On the other hand, if the sample crystallinity is low, the D_{TEM} corresponds better to the particle diameter as calculated from the BET surface area (D_{BET}) (Table 2). Hence, particles consisting of several interfaced crystallites (i.e., rounded larger shapes) gives a D_{TEM} size closer to the volume-averaged D_{BET} particle size.

3.5. Morphology and Structure. A careful investigation by HREM, supported by X-ray diffraction and X-ray photoelectron spectroscopy, are excellent complementary methods to explore the morphological phenomena of poorly crystalline composites, which we show[32] can reveal information about the redox mechanisms involved during catalysis.

Several explanations that describe the morphology and how the copper species interact with the ceria are found in the literature and are briefly summarized below. It should be emphasized that the observed inconsistency is often due to the use of different preparation methods. It might be expected that the Cu−CeO_2 system would behave similarly to the Cu−ZrO_2 system.[74] In fact, it has been shown[20,47,59,66,75] that small amounts of copper ions may be introduced in the fluorite-type ceria lattice, which is followed by a contraction of the unit cell if the inclusion proceeds in a structurally ordered mode. For example, Jiang et al.[47] and Lamonier et al.[59] explain the system as solid solution of Cu^{2+} in ceria in contact with copper oxide crystals of variable size. Fernadez-García et al.[20] explain it by assuming the existence of a mixed perovskite phase involving the substitution of Ce^{4+} by Cu^{1+}, while the charge compensation may be achieved via the partial oxidation of the remaining Ce^{3+} ions or by the creation of oxygen vacancies. Another group of authors[9,13,17,23,76] propose a substitutional solid solution and the coexistence of two redox couples (Ce^{4+}, Ce^{3+} and Cu^{2+}, Cu^{1+}), but only at the interfacial area of copper oxide and ceria crystals that would leave the unit cell unaffected according to XRD. Hocevar et al.[23] have, however, demonstrated two different explanations depending on the preparation method. First (i), coprecipitated samples can be described as a two-phase system; one phase is cerianite composed with interstitial Cu^{1+} ions, which is shown to cause a unit cell contraction of more than 1% for a 20 at. % load, and the second phase is bulk CuO. Sol−gel-prepared samples, second (ii), contain only finely dispersed CuO clusters (i.e., X-ray amorphous) on the surface of poorly crystalline CeO_2 particles. In this case, the authors propose that a thin film of a copper solid solution is "sandwiched" between the dispersed CuO clusters and CeO_2 crystallites, for which a diffraction line shift cannot be detected by XRD. The sol−gel-prepared sample was reported to exhibit a 4 times higher conversion rate for the oxidation of carbon monoxide compared to the coprecipitated one. This is in agreement with others,[38,39,72] also reporting that Cu/Ce/O catalysts with a higher degree of structure disorder (X-ray amorphous) exhibit higher catalytic activities for the CO oxidation. It is known that nanocrystallites and amorphous material are more easily reduced,[23,39,69] and oxidized,[19] than microcrystalline materials.

(72) Craciun, R. *Solid State Ionics* **1998**, *110*, 83.
(73) Li, C.; Sakata, Y.; Arai, T.; Domen, K.; Maruya, K.-I.; Onishi, T. *J. Chem. Soc., Faraday Trans. 1* **1989**, *85* (4), 929 (part 1); **1989**, *85* (6), 1451 (part 2).
(74) Dongare, M. K.; Ramaswamy, V.; Gopinath, C. S.; Scheurell, S.; Brueckner, M.; Kemnitz, E. *J. Catal.* **2001**, *199*, 209.
(75) Terrible, D.; Trovarelli, A.; Leitenburg de, C.; Primavera, A.; Dolcetti, G. *Catal. Today* **1999**, *47*, 133.
(76) Aboukaïs A.; Bennani, A.; Aïssi, C. F.; Wrobel, G.; Guelton, M. *J. Chem. Soc., Faraday Trans* **1992**, *88*, 1321.

For medium copper contents (6−25%), we have shown by HED that the amount of Cu in our IGC-produced samples cannot be recovered by a CeO_2 lattice incorporation of copper ions. Neither can it be explained by crystalline CuO inclusions because none were detected by HED and EFTEM. Furthermore, the XPS and HED results also indicate an optimum surface dispersion of copper and a slightly reduced material. We therefore would like to assign our system to a modified version of Hocevar et al.'s[23] explanation (ii): Highly dispersed CuO clusters (X-ray amorphous) on the surface of CeO_2 nanocrystallites, which at the interface forms a thin film of a substitutional $Ce_{1-x}Cu_xO_{2-\delta}$ solid solution, undetectable by X-ray diffraction. Thus, during catalysis at elevated temperatures, the coexistence of the two-redox couples, Ce^{4+}/Ce^{3+} and Cu^{2+}/Cu^{1+}, may exist at very high concentrations at the boundaries of the nanocrystalline ceria. The best catalytic activity for the combustion of carbon monoxide can therefore be expected for the catalysts exposing this kind of material properties (Group B).

4. Conclusions

By employing the inert gas condensation technique, we have produced nonstoichiometric CuO_x/CeO_2 nanocomposite powders, for which the composition was altered successfully over the entire range (2−98% Cu). Experiments were carried out using various multiple crucible configurations of the Cu and Ce metal sources as this has been considered to be of major importance. We suggest that when the Cu crucible(s) are positioned closer than the Ce crucible(s) to the collective coldfinger, only very small clusters (i.e., monomers/oligomers) can form before collision and aggregation with larger cerium clusters is initiated. During the following oxygen treatment, this will ensure a high copper dispersion on CeO_2, which acts as an effective synergistic support and prevents the formation of bulk CuO. However, the factors that have the highest impact on the resulting particle morphology were ascribed to the helium pressure and the composition of the composite. During the synthesis a 1.0 Torr helium pressure was found to be the most favorable condition for controlling the composition and particle growth. The crystallite size was most sensitive for changes in the pressure range 0.5−5 Torr He, while the particle size, constituting of several aggregated crystallites, was shown to increase significantly at pressures above 5 Torr of He.

At low copper contents (Group A; <6%) the particles consist of epitaxially agglomerated nanocrystallites of CeO_2. Rounded particle shapes consisting of epitaxially interfaced crystallites occur more frequently in poorly crystalline samples (X-ray amorphous), while block shapes exhibiting sharp edges and distinct flat surfaces are more common in samples with higher X-ray crystallinity. A high X-ray crystallinity gives a D_{TEM} comparable to the single-crystallite size D_β. Conversely, a low X-ray crystallinity gives a D_{TEM} that is close to the volume-averaged D_{BET}.

For medium copper contents (Group B; 6−25%) the catalyst samples exhibit a uniform morphology with a narrow particle size distribution. No direct evidence for crystalline CuO_x was found by HREM, but the XPS measurements showed that the copper species are predominately located, and evenly distributed, on the surface of the CeO_2 nanocrystalline aggregates. The copper species are thereby more easily accessible for CO adsorption. We suggest that a thin film of a substitutional solid solution (X-ray amorphous), and coexistence of the two redox couples, Ce^{4+}/Ce^{3+} and Cu^{2+}/Cu^{1+}, exist in a high concentration at the boundaries of the nonstoichiometric nanocrystallites that would give it excellent catalytic properties.

For high copper contents (Group C; 25−70%) a large number of samples showed crust structures. We present a model that illustrates the growth mechanism, and which also may explain the observed extreme dispersion of copper on ceria. The formation of crust structures is attributable to a sequential oxidation of Ce followed by Cu and to an ideal proportion of lattice expansion for the oxides. Contrarily to the catalysts prepared by, for example, impregnation, the copper dispersion showed no signs of surface saturation. Nevertheless, a surface discrimination of copper relative to cerium was noted by XPS above ≈20% Cu. The copper species appear thus to be amorphously "sandwiched" between the CeO_2 crystal boundaries because the total area of internal boundaries, undetectable by XPS, always is larger than the exposed surface area. Above 30% Cu, bulk CuO (tenorite) is detected by HED, but according to the high-resolution elemental mapping (EFTEM) results, the major part of the copper is observed to be still highly dispersed. Nevertheless, for copper contents exceeding 30%, the cerium dioxide surface will assist the formation of fully oxidized CuO particles, as the extreme dispersion of copper oxide cannot be totally preserved.

At very high copper contents (Group D; >70%), the aggregate particles display a generally amorphous character with crystallites of ceria evenly distributed. The low amount of cerium oxide is not adequate to ensure an effective dispersion and oxidation of the copper, which consequently gives larger particles of Cu or Cu_2O (>97% Cu).

We show a slight reduction of the surface (by XPS) as well as the bulk (by HED) of the CuO_x/CeO_2 nanocomposite particles, which verifies that reduced copper species can be stabilized on the surface and boundaries of ceria nanocrystals even at room temperature. Whether the reduced copper species on fresh samples can have a positive effect on the catalytic activity is still unclear, but it indicates that the ceria structure can assist redox processes during a catalytic event. In a following paper,[32] in which we focus more on the catalytic results, EXAFS measurements confirm the existence of slightly reduced and amorphous copper oxide.

This study has demonstrated the uniqueness of inert gas synthesis as well as the applicability of high-resolution TEM to distinguish catalytic material properties beyond reach for analytical X-ray techniques alone in advanced model catalyst characterization.

Acknowledgment. Support from the Sweden-Japan foundation, the Swedish Natural Science Research Council, and the EU supported TMR network CLUPOS (Contract FMRX-CT98-0177) are gratefully acknowledged. The ESRF facility in Grenoble, France, is acknowledged for the high-energy diffraction experiments at ID15B.

CM021101U